Crop Yield Estimation Based on Unsupervised Linear Unmixing of Multidate Hyperspectral Imagery

Bin Luo, Chenghai Yang, Jocelyn Chanussot, *Fellow, IEEE*, and Liangpei Zhang, *Senior Member, IEEE*

Abstract—Hyperspectral imagery, which contains hundreds of spectral bands, has the potential to better describe the biological and chemical attributes on the plants than multispectral imagery and has been evaluated in this paper for the purpose of crop yield estimation. The spectrum of each pixel in a hyperspectral image is considered as a linear combinations of the spectra of the vegetation and the bare soil. Recently developed linear unmixing approaches are evaluated in this paper, which automatically extracts the spectra of the vegetation and bare soil from the images. The vegetation abundances are then computed based on the extracted spectra. In order to reduce the influences of this uncertainty and obtain a robust estimation results, the vegetation abundances extracted on two different dates on the same fields are then combined. The experiments are carried on the multidate hyperspectral images taken from two grain sorghum fields. The results show that the correlation coefficients between the vegetation abundances obtained by unsupervised linear unmixing approaches are as good as the results obtained by supervised methods, where the spectra of the vegetation and bare soil are measured in the laboratory. In addition, the combination of vegetation abundances extracted on different dates can improve the correlations (from 0.6 to 0.7).

Index Terms—Airborne hyperspectral imagery, crop yield, grain sorghum field, multidate, unmixing.

I. INTRODUCTION

REMOTELY sensed imagery is widely used for the estimation of the yields of crop fields. Traditionally, multispectral imagery, which contains several spectral bands covering visible and near-infra-red wavelengths, are used for the purpose of vegetation monitoring [1]–[4]. Vegetation indices have been proven to be a useful tool for crop yield estimation (e.g., [5]–[10]). Different approaches have also been applied (such as neural network [11] and autoregressive models [12]), with moderate success.

Hyperspectral imagery, which contains hundreds of spectral bands, has been evaluated for crop parameter estimations (crop

B. Luo is with the State Key Laboratory of Information Engineering in Surveying, Mapping and Remote Sensing (LIESMARS), Wuhan University, Wuhan 430079, China, and also with the Department of Image and Signal, GIPSA-Lab, 38401 Grenoble, France (e-mail: robinlb2002@gmail.com).

C. Yang is with USDA-ARS, Southern Plains Agricultural Research Center, College Station, TX 77845 USA (e-mail: Chenghai.Yang@ars.usda.gov).

J. Chanussot is with the Department of Image and Signal, GIPSA-Lab, 38401 Grenoble, France (e-mail: jocelyn.chanussot@gipsa-lab.grenoble-inp.fr).

L. Zhang is with the State Key Laboratory of Information Engineering in Surveying, Mapping and Remote Sensing (LIESMARS), Wuhan University, Wuhan 430079, China.

Color versions of one or more of the figures in this paper are available online at http://ieeexplore.ieee.org.

Digital Object Identifier 10.1109/TGRS.2012.2198826

chlorophyll for example [13]–[16]) and crop yield estimation [17]–[21]. These almost continuous spectra, which provide much more spectral information on the observation scenes, have the potential to better describe the biological and chemical attributes on the plants than multispectral imagery [22]. The spectrum of a pixel in a hyperspectral image is a mixture of the spectra of some basic components (thereafter called *endmembers*). By unmixing the spectrum of each pixel, one can compute the spatial abundances of the endmembers. Moreover, the spatial abundance of the vegetation on a scene derived from a hyperspectral image can be more precise than the vegetation index deduced from a multispectral image. Recently, the authors of [23] propose to compute the vegetation abundance to map the yield of sorghum fields using linear unmixing of hyperspectral images. The correlation coefficients between the vegetation abundances and the yield data are quite satisfactory. The authors suppose that the spectrum of a pixel in the hyperspectral image on a crop field is a linear mixture of the spectra of vegetation and bare soil. The abundance of vegetation is then calculated by using linear unmixing. In [23], the spectra of vegetation and bare soil are supposed to be known, which are either measured in laboratory or selected manually from the image. However, the reference spectra are not always available; or they are difficult to obtain.

The first contribution of this paper is to evaluate unsupervised linear unmixing approaches for hyperspectral images for crop yield estimation, which do not need any reference spectra. For unsupervised linear unmixing of hyperspectral images, one can find two types of approaches [24]: statistical methods (such as the independent component analysis (ICA) [25] and Bayesian positive source separation (BPSS) [26]) and geometrical methods. Reviews and assessments of these unmixing methods can be found in [27] and [28]. The statistical methods extract the endmembers by optimizing some statistical criteria. For example, the independence between the endmembers is assumed for ICA. However, either these statistical criteria are not always valid for hyperspectral images, or the statistical methods, such as BPSS, which perform Monte Carlo simulations for obtaining the endmembers, are extremely slow. The geometrical approaches are based on the geometrical properties of linear mixture model of hyperspectral data. These methods are more adaptive to the data and are generally more effcient. They can be devided into two classes: direct methods (such as N-Finder [29], vertex component analysis (VCA) [30], and sequential maximum angle convex cone (SMACC) [31]) and advanced methods (for example minimum volume constrained nonnegative matrix factorization (MVCNMFT) [32], minimum volume enclosing simplex (MVES) [33], simplex identification

via split augmented lagrangian (SISAL) [34], and minimum volume simplex analysis (MVSA) [35]). The direct methods extract the extremal points within the data set as endmembers. They are very efficient. However, they assume that for each endmember, there is at least one pure pixel in the image (pure pixel assumption). Otherwise, the extracted endmembers by these methods are still mixed pixels. The advanced methods either try to find the simplex with minimum volume which contains all data points and extract the extremal points of the simplex as endmembers (such as MVES, SISAL, and MVSA); or minimize the projection error of the data to a subset and use the simplex volume as a regularization term (such as MVCNMFT). In this paper, the endmembers are mainly extracted by direct methods (VCA and N-Finder). This choice is based on the fact that, at first these two methods are quite efficient. Second, the spatial resolutions of the images are quite high, the pure pixel assumption can be satisfied. For the reason of comparison, one advanced method MVSA has also been evaluated. In addition, the spatial preprocessing proposed in [36] which allows to enhance the endmembers is also evaluated in this paper. With the help of the unsupervised unmixing scheme, we can obtain the abundance map of vegetation without any manual processing and any information *a piori* on the crop.

The second contribution of this paper is to use the hyperspectral images of the same fields taken on two different dates for yield estimation. Even though the images are often taken in good observation conditions (sunny and calm weather), the light and weather can still have influence on the observation. In addition, calibration errors can randomly occur in an image. Thus, the relations between the yield data and different observations will vary [9]. The fusion of different independent observations on the same scene can reduce the influences of this uncertainty and obtain a robust result. In this paper, we propose several fusion approaches in order to combine, for each field, the unmixing results obtained on two different dates in order to improve the accuracy of the estimation.

The outline of this paper is as follows. In Section II, we present briefly the linear mixture models of hyperspectral images and the used linear unmixing approaches in this study. In Section III, we briefly present the used data sets. In Section IV, several fusion schemes are proposed for combining the unmixing results obtained on multidate hyperspectral images. In Section V, the protocols of the experiments are presented. In Section VI, we present the mapping results obtained on real hyperspectral data sets. In Section VII, we have compared the results obtained by two advanced unmixing techniques: the MVSA method which does not require pure pixels and the spatial preprocessing for enhancing the endmembers. Finally, we conclude in Section VIII.

II. LINEAR UNMIXING OF HYPERSPECTRAL IMAGES

We note $\mathbf{X}$ the matrix representing the hyperspectral image cube, where $\mathbf{X} = \{\mathbf{x}(1), \mathbf{x}(2), \ldots, \mathbf{x}(N_a)\}$ and $\mathbf{x}(k) = \{x(1, k), x(2, k), \ldots, x(N_s, k)\}^T$, $x(l, k)$ is the value of the kth pixel at the lth band, N_s is the number of spectral bands and N_a is the number of pixels. We assume that the spectrum of

each pixel is a linear mixture of the spectra of N_c endmembers, leading to the following model:

$$\mathbf{X} = \mathbf{MS} + \mathbf{n} \tag{1}$$

where $\mathbf{M} = \{\mathbf{m}(1), \mathbf{m}(2), \ldots, \mathbf{m}(N_c)\}$ is the mixing matrix where $\mathbf{m}(n)$ denotes the spectral signature of the nth endmember. $\mathbf{S} = \{\mathbf{s}(1), \mathbf{s}(2), \ldots, \mathbf{s}(N_c)\}^T$ is the abundance matrix where $\mathbf{s}(n) = \{s(n, 1), s(n, 2), \ldots, s(n, N_a)\}$ $(s(n, k) \in [0, 1]$ is the abundance of the nth endmember at the kth pixel). $\mathbf{n}$ stands for the additive noise of the image. Two main assumptions could be made on the endmembers:

- non-negativity: the spectra $\mathbf{M}$ and the abundances $\mathbf{S}$ are non-negative;
- sum-to-one: $\sum_{n=1}^{N_c} s(n, k) = 1$; the sum of the abundances of all the endmembers at the same pixel should be one.

Since the abundances of the endmembers conform to the positivity and sum-to-one conditions, the hyperspectral data should be limited inside the simplex formed by the endmembers, if the data is noise free. Therefore, the extrema of the simplex formed by the hyperspectral data are endmembers. Based on this property, lots of geometrical linear unmixing approaches are proposed, such as PPI [37], n-Finder [29], VCA [30], and SMACC [31].

Among these approaches, we use N-Finder and VCA methods for unmixing the hyperspectral images, which are the most efficient and the most widely used.

N-Finder searches the simplex embedded inside the data sets, of which the volume is maximal. The extremities of this simplex are extracted as endmembers. As initialization of the simplex, N-Finder selects a given number of random points. It iteratively replaces the original points by new points. If the new points increase the volume of the simplex, it keeps the new points. The iterations stop when the simplex does not enlarge. In this paper, the dimensionality reduction step required by N-Finder is realized by singular value decomposition.

VCA iteratively projects the data onto the direction orthogonal to the subspace spanned by the already determined endmembers. The extremity of this projection is the new endmember signature. VCA stops the iterations when the desired number of endmembers are attained.

N-Finder and VCA are very similar, because they all try to find the extremities of the simplex formed by the data points. However, it has to be noticed that the computational complexity of N-Finder is much larger than VCA.

For each hyperspectral image taken on the field, we extract two endmembers (soil and vegetation) by either N-Finder or VCA. Once the spectra of these endmembers are extracted, the abundances of the endmembers are estimated by using two strategies. The first strategy minimizes the error between the hyperspectral data and the linear reconstruction, which subjects to the non-negative condition. More concretely, the abundances of the endmembers are obtained by

$$\hat{\mathbf{S}}_{Nnls} = \arg\min_{\mathbf{S}} \|\mathbf{X} - \mathbf{MS}\|^2,$$

$$s.t. \quad \mathbf{S} \geq 0. \tag{2}$$

The second one minimizes the error, which subjects to the non-negativie and sun-to-one condition. More concretely, the abundances of the endmembers are obtained by

$$\hat{\mathbf{S}}_{Fcls} = \arg\min_{\mathbf{S}} \|\mathbf{X} - \mathbf{MS}\|^2,$$

$$s.t. \quad \mathbf{S} \geq 0 \quad \text{and} \quad \sum_{n=1}^{N_c} s(n,k) = 1. \tag{3}$$

III. DATA SETS

A. Hyperspectral Images

Two irrigated sorghum fields in south Texas are considered in this paper. They are noted as Field 1 and Field 2, of which the areas are, respectively, 13.4 and 14.0 ha. The soil is mainly Delfina loamy fine sand. Grain sorghum is normally cultivated in rotation. For these two fields, sorghum (AgriPro 9850) was planted in late February 2001 and harvested in late June of the same year.

The imagery was acquired from the fields with a hyperspectral imaging system mounted on a Cessna 206 aircraft. Raw data were recorded with 12-bit and 128 spectral bands from 457.2 to 921.7 nm at spectral resolution of 3.63 nm. No stabilizer or inertial measurement device was mounted on the aircraft for measuring the variation. The geometrical distortions were corrected by using a reference line approach presented in [38]. Since the quantum efficiency near the NIR end of the spectrum is low, reflectances for wavelengths larger than 846 nm were unreliable. And the first few bands of the blue region are very noisy. Therefore, bands 1–5 and 108–128 were removed, and the remaining 102 bands were used for experiments.

The flight height was 1680 m above ground level, and the speed was 150 km/h. The swath of the imagery was approximately 840 m with a 1.3 m spatial resolution. GPS data were collected for image registration. For each field, hyperspectral images were recorded on two different dates (18 May 2001 and 29 May 2001) under sunny and calm conditions. The crop had reached the soft to hard dough stages and had achieved its maximum canopy cover. The hyperspectral images taken on the two fields of different dates are shown in Fig. 1.

B. Crop Yield Data

Yield data were recorded by an Ag Leader PF3000 yield monitor (Ag Leader Technology, Ames, Iowa). Yield, moisture, and location were recorded at the same time. The combine used had a cutting width of 8.7 m. The yield and GPS data were preprocessed before experiments. An optimum time lag of 15 s was used to align the yield with location, and the yield data were adjusted to 14% moisture content.

The crop yield data have the same coordinate system as the images. Notice that the spatial resolution of the hyperspectral images are 1 m; therefore, the yield data were interpolated to the same resolution as the images by using bilinear interpolation.

It has to be noticed that even though the geometrical distortions in the images were corrected, there were still residues (geometrical calibration errors) and there were small variations
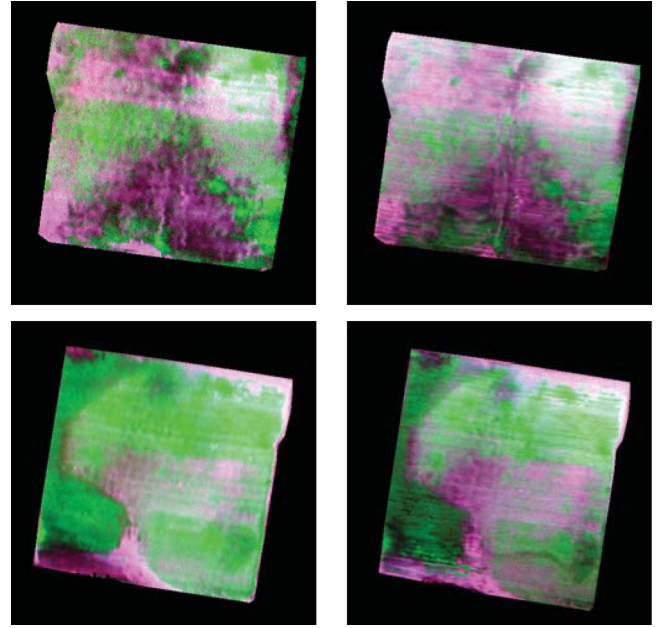

Fig. 1. (Top) Hyperspectral images of Field 1 (R-band 55, G-band 85, B-band 30) taken, respectively, on 18 May 2001 (left) and on 29 May 2001 (right). (Bottom) Hyperspectral images of Field 2 (R-band 55, G-band 85, B-band 30) taken, respectively, on 18 May 2001 (left) and on 29 May 2001 (right).
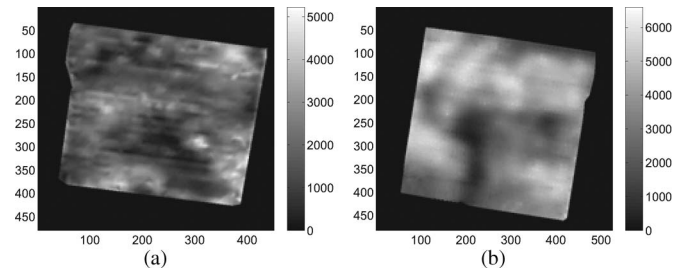

Fig. 2. Crop yield maps of the two fields. In order to compare with the results of the linear unmixing, the crop yield maps are interpolated to 1 m resolution by bilinear interpolation. (a) Field 1. (b) Field 2.

in the observation conditions on the two dates. The variations are mainly due to the slight difference of the crop growth stage between the two dates. Plants were at the soft dough stage on the first imaging date and at the hard dough stage on the second date. Therefore, a fusion of the observation results of the same fields taken on different dates might be able to improve estimation results (Fig. 2).

IV. FUSION OF UNMIXING RESULTS OF MULTIDATE HYPERSPECTRAL IMAGES

Though the images are often taken in good observation conditions (sunny and calm weather), the light and weather can still have influence on the observation. In addition, calibration errors, noise can randomly occur in an image [9]. In order to reduce the influences of this uncertainty and obtain a robust result, the fusion of different independent observations on the same scene is proposed. The fusion can be done by two families of operations. One is based on simple arithmetics of the vegetation

abundances computed on different dates, while another is based on their weigthed combinations. In order to find the best way of fusion, we propose 13 approaches, among which seven are based on simple arithmetics and six are based on weigthed combinations with weights determined by the reconstruction signal-to-noise ratios (SNR) of the linear unmixing.

From the hyperspectral image of a given field taken on a given date, the spectra and the abundances of two endmembers are extracted by either VCA or N-Finder. We then identify the endmember corresponding to the vegetation. For each field, we note $M_{18}(k)$ and $M_{29}(k)$ as the abundances of vegetations extracted on the date 18 May 2001 and 29 May 2001 at the kth pixel, respectively.

We first propose seven combinations of vegetation abundances based on simple arithmatics of M_{18} and M_{29}. For comparison purpose, the first two combinations are effectively the original vegetation abundances computed on one single date. The seven combinations are defined by

$$M_1(k) = M_{18}(k) \tag{4}$$

$$M_2(k) = M_{29}(k) \tag{5}$$

$$M_3(k) = M_{18}(k) + M_{29}(k) \tag{6}$$

$$M_4(k) = M_{18}(k)^2 + M_{29}(k)^2 \tag{7}$$

$$M_5(k) = (M_{18}(k) + M_{29}(k))^2 \tag{8}$$

$$M_6(k) = M_{18}(k)M_{29}(k) \tag{9}$$

$$M_7(k) = \sqrt{M_{18}(k)M_{29}(k)}. \tag{10}$$

We then propose six weighted combinations of vegetation abundances computed on different dates, of which the weights are based on the reconstruction SNR. We note $SNR_{18}(k)$ and $SNR_{29}(k)$ the SNR of the reconstruction by using unmixing results at the kth pixel. More concretely, let $x_{18}(l, k)$ represent the value at the kth pixel and on the lth spectral band of the original hyperspectral image taken on the date 18 May 2001; and $\hat{x}_{18}(l, k)$ represent the pixel value at the same band and the same location on the reconstructed image by using the spectra and the abundances of the extracted endmembers, then

$$SNR_{18}(k) = 10 \log_{10} \frac{\sum_{l=1}^{N_s} \|x_{18}(l, k)\|^2}{\sum_{l=1}^{N_s} \|x_{18}(l, k) - \hat{x}_{18}(l, k)\|^2}. \tag{11}$$

The SNR of the reconstructions are used as weights in order to combine the vegetation abundances. The main idea is to add more abundances extracted on the date where the reconstruction SNR is relatively high.

The six combinations are defined by

$$M_8(k) = D(k)M_{18}(k) + (1 - D(k)) M_{29}(k) \tag{12}$$

$$M_9(k) = M_{18}(k)^{D(k)} M_{29}(k)^{1-D(k)} \tag{13}$$

$$M_{10}(k) = D(k)M_{18}(k)^2 + (1 - D(k)) M_{29}(k)^2 \tag{14}$$

$$M_{11}(k) = M_{18}(k)^{2D(k)} M_{29}\left(i, j^{2-2D(k)}\right) \tag{15}$$

$$M_{12}(k) = T(k)M_{18}(k) + (1 - T(k)) M_{29}(k) \tag{16}$$

$$M_{13}(k) = T(k)M_{18}(k)^2 + (1 - T(k)) M_{29}(k)^2 \tag{17}$$

where

$$D(k) = \frac{d(k) - \inf(d(k))}{\sup(d(k)) - \inf(d(k))} \in [0, 1]$$

$$d(k) = SNR_{18}(k) - SNR_{29}(k)$$

$$T(k) = \begin{cases} 1, & SNR_{18}(k) > SNR_{29}(k) \\ 0, & otherwise. \end{cases}$$

Notice that the combined abundances M_3 (resp. M_4, M_6, M_7) are effectively a special case of M_8 (resp. M_{10}, M_9, M_{11}) when we set $D(k) = 0.5, \forall k$.

V. PROTOCOLS OF THE EXPERIMENTS

The two approaches (VCA and N-Finder) presented in Section II have been used to unmix the hyperspectral images taken on the sorghum fields on two dates. For each image, the spectra of two endmembers (vegetation and soil) are automatically extracted by the two methods. Their abundance maps will then be computed by using two strategies: the one with only non-negative condition [see (2)] and the one with both non-negative and sum-to-one conditions [see (3)]. We then identify the endmember corresponding to the vegetation. The vegetation abundance and combined vegetation abundances obtained on the two dates [see (4)–(17)] are then compared with the interpolated crop yield maps. According to the linear mixture model (see Section II) of hyperspectral images, the values of the abundance maps reflect the relative variabilities of the endmembers; it is impossible to compare their absolute values with the crop yield data. Therefore, we compute the correlation coefficients between the (combined) vegetation abundances and the yield data by the following equation:

$$C(M_i, Y) = \frac{Cov(M_i, Y)}{\sigma_{M_i} \sigma_Y}, \quad i = 1, 2, \ldots, 13 \tag{18}$$

where $Cov(M_i, Y)$ is the covariance value between the (combined) vegetation abundance M_i [computed by one of the (4)–(17)] and the yield data Y; σ_{M_i} and σ_Y are the standard deviation of M_i and Y, respectively. For each field, there will be 52 correlation coefficients computed between the (combined) vegetation abundances and the yield data (two endmember extraction approaches $\times$ two unmixing stradegies $\times$ 13 (combined) vegetation abundances).

VI. RESULTS

A. Results on Field 1

1) Endmembers: In Fig. 3(a) and (b), we show the spectra of the two endmembers extracted by using VCA and N-Finder on the image of Field 1 taken on the date 18 May 2001. It can be seen that the endmembers extracted by the two methods are quite similar and that the first endmember extracted by VCA, the second endmember extracted by N-Finder corresponds to vegetation.

In Fig. 3(c) and (d), we show the spectra of the two endmembers extracted by using VCA and N-Finder on the image of Field 1 taken on the date 29 May 2001. It can be seen that the
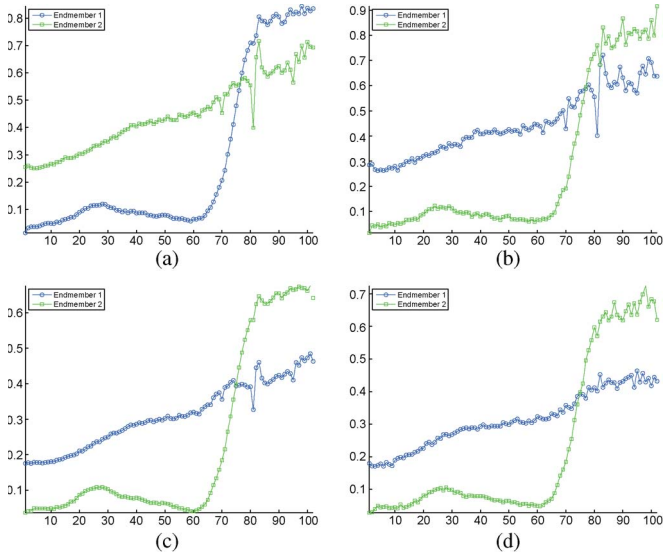
Fig. 3.   Spectra of the two endmembers extracted by using VCA and N-Finder on the image of **Field 1** taken on 18 May 2001 (top row) and 29 May 2001 (bottom row).
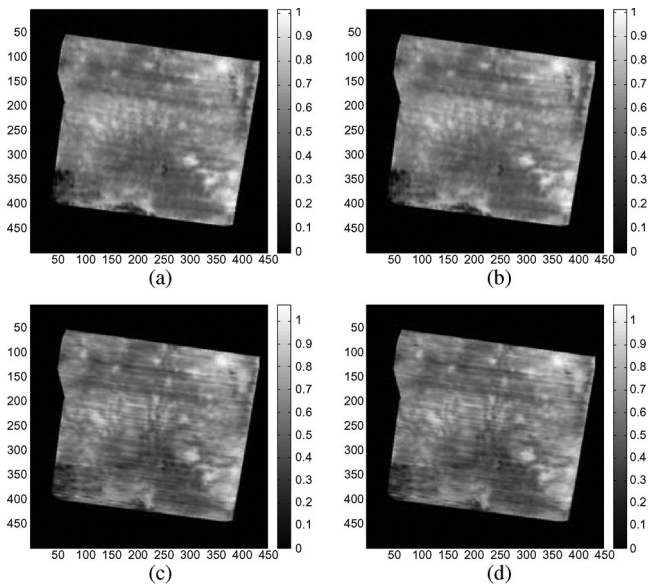

Fig. 4.   Abundances of the vegetation endmembers extracted by using VCA and N-Finder on the image of **Field 1** taken on 18 May 2001 (top row) and 29 May 2001 (bottom row). The abundances are estimated with non-negative condition [see (2)].

second endmember extracted by VCA and the first endmember extracted by N-Finder correspond to vegetation.

2) Abundance Maps Obtained With Non-Negative Condition: With the help of the spectra of the endmembers extracted by VCA and N-Finder, in this paragraph, we compute the abundances of these endmembers by using (2). In Fig. 4, we show the vegetation abundance maps of the endmembers extracted by VCA and N-Finder on the image of Field 1 taken on the dates of 18 May 2001 and 29 May 2001.

It can be seen from Fig. 4 that the abundances of vegetation endmembers extracted by both VCA and N-Finder are very similar to the crop yield map, which confirms the vegetation
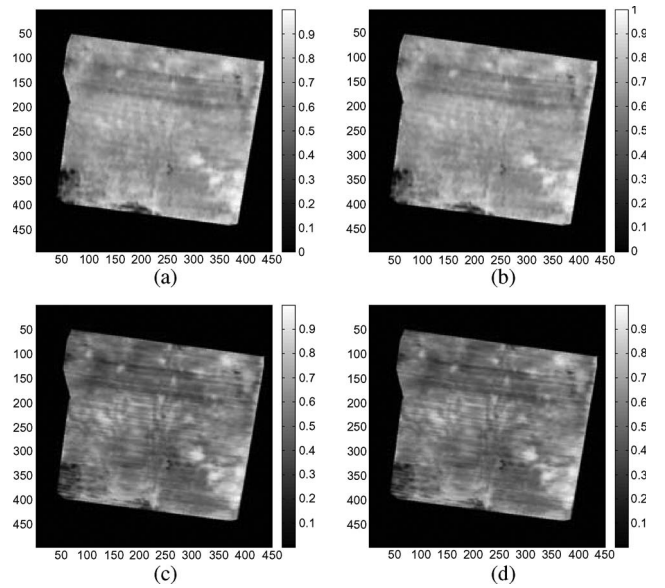

Fig. 5.   Abundances of the vegetation endmembers extracted by using VCA and N-Finder on the image of **Field 1** taken on 18 May 2001 (top row) and 21 May 2001 (bottom row). The abundances are estimated with non-negative and sum-to-one conditions [see (3)].

identification by the spectra of the extracted endmembers according to Fig. 3.

3) Abundance Maps Obtained With Non-Negative and Sum-to-One Conditions: In this paragraph, we compute the abundances of the endmembers by using (3). In Fig. 5, we show the abundance maps of the endmembers extracted by VCA and N-Finder on the image of Field 1 taken on the dates of 18 May 2001 and 29 May 2001.

From Fig. 5, the identifications of the endmembers corresponding to vegetation are confirmed. However, it can be observed that when the abundances are computed with both non-negative and sum-to-one conditions, the similarities between the vegetation abundances and the interpolated yield map are much worse than the vegetation abundances computed with only non-negative condition. This may be due to the over-fitting when the two constrains are both used.

4) Correlation Coefficients Between the (Combined) Vegetation Abundances and the Interpolated Yield Map of Field 1: We then compute the correlation coefficients between the crop yield map of Field 1 with the (combined) vegetation abundances computed by (4)–(17). The results are shown in Table I.

Four remarks could be drawn from these results:

- The abundance maps (M_1 and M_2) computed with only non-negative condition are strongly correlated to the yield map (more than 0.7, which are already higher than the best correlation coefficients obtained by the state-of-art method presented in [23]). The unsupervised unmixing methods have better performances than the supervised approach presented in [23]. The correlation coefficients obtained on the abundance maps computed with both non-negative and sum-to-one conditions are relatively low (around 0.5–0.6).
- The performances of both VCA and N-Finder are very similar. When the abundances are computed by using (2),

TABLE I
CORRELATION COEFFICIENTS BETWEEN THE INTERPOLATED CROP YIELD MAP AND THE (COMBINED) VEGETATION ABUNDANCES COMPUTED BY (4)–(17) ON THE IMAGE OF **Field 1**. FOR FIRST THREE COLUMNS, THE ABUNDANCES ARE COMPUTED WITH NON-NEGATIVE CONDITION. WHILE FOR LAST THREE COLUMNS, THE ABUNDANCES ARE COMPUTED WITH BOTH NON-NEGATIVE AND SUM-TO-ONE CONDITIONS

| Non-negative condition												
	M_1	M_2	M_3	M_4	M_5	M_6	M_7	M_8	M_9	M_{10}	M_{11}	M_{12}	M_{13}
VCA	0.739	0.748	0.768	0.784	0.782	0.780	0.764	0.769	0.766	0.786	0.783	0.748	0.763
N-Finder	0.738	0.743	0.765	0.781	0.779	0.777	0.761	0.760	0.756	0.777	0.774	0.730	0.746
Non-negative and sum-to-one conditions												
	M_1	M_2	M_3	M_4	M_5	M_6	M_7	M_8	M_9	M_{10}	M_{11}	M_{12}	M_{13}
VCA	0.577	0.749	0.707	0.727	0.733	0.738	0.711	0.743	0.746	0.765	0.773	0.706	0.727
N-Finder	0.575	0.752	0.708	0.729	0.734	0.739	0.712	0.748	0.750	0.769	0.776	0.705	0.726
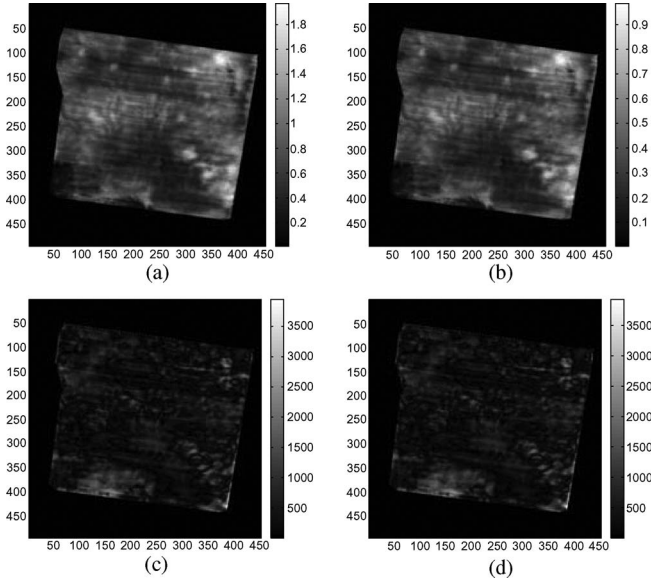
Fig. 6. (a) M_4 and (b) M_{10} computed on **Field 1**. The endmembers are extracted by VCA, and the abundances are computed with (2). They are the most correlated with the yield map of Field 1. (c) and (d) Absolute error between the yield map and the fitted model $\hat{Y}_4, \hat{Y}_{10}$ [see (19)].
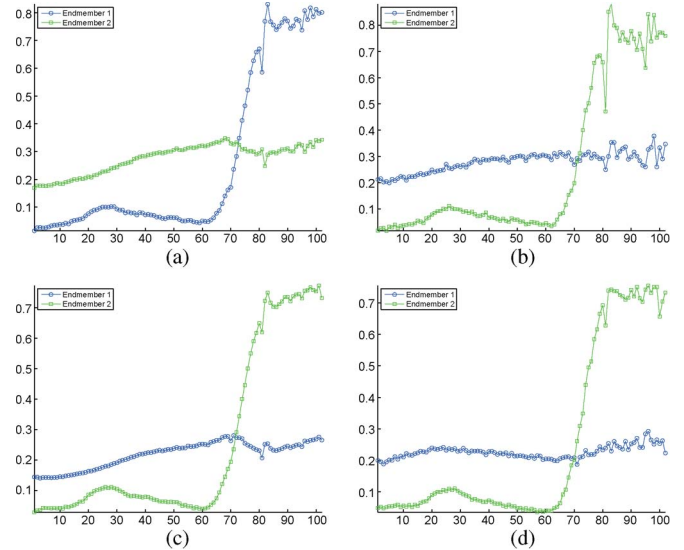

Fig. 7. Spectra of the two endmembers extracted by using VCA and N-Finder on the image of **Field 2** taken on 18 May 2001 (top row) and 29 May 2001 (bottom row).

the results of VCA are slightly better. While when the abundances are computed by using (3), it is inverse.

- By combining the vegetation abundances of the two dates, the correlation coefficients improve. We can see that the highest correlation coefficients (around 0.78, which are higher than the results in [23]) are obtained among M_4, M_5, M_6, M_{10}, and M_{11} [see (7)–(9), (14), and (15)], where M_4, M_5, and M_6 are simple combinations of the abundances on the two dates and M_{10}, M_{11} are weighted combinations when the SNR of reconstructions are taken into consideration. Even when the abundances are computed by using (3), these combined vegetation abundances (M_4, M_5, M_6, M_{10}, and M_{11}) can provide relatively high correlation coefficients.
- The highest correlation coefficients are obtained by M_4 and M_{10} when the endmembers are extracted by VCA and the abundances are computed with only non-negative condition [see (2)]. Remark that M_4 is in fact a special case of M_{10} when $D(k) = 0.5, \forall k$. The sum of the square of the two vegetation abundances are the most correlated to the yield map, and when the SNR of reconstruction is taken into consideration, the correlation coefficient is slightly better.

In Fig. 6(a) and (b), we show the combined vegetation abundances computed on Field 1 of which the correlation coefficients are the highest (M_4 and M_{10} when the endmembers are extracted by VCA and the abundances are computed with only non-negative condition).

We then fit the two combined vegetation abundances (M_4 and M_{10}) with the yield map by linear regression. More concretely, we compute the fitted model $\hat{Y}_i(k)$ by

$$\hat{Y}_i(k) = \hat{\alpha}_i + \hat{\beta}_i M_i(k), \quad i = 4, 10 \qquad (19)$$

where

$$\{\hat{\alpha}_i, \hat{\beta}_i\} = \arg \min_{\alpha_i, \beta_i} \left\{ \sum_k \left\| \hat{Y}_i(k) - Y(k) \right\|^2 \right\}.$$

The absolute error between $\hat{Y}_4(k)$ (resp. $\hat{Y}_{10}$) and the yield map $Y(k)$ by $E_4(k) = |\hat{Y}_4(k) - Y(k)|$ (resp. $E_{10}(k) = |\hat{Y}_{10}(k) - Y(k)|$), which is shown in Fig. 6(c) [resp. 6(d)].

It can be seen that the errors are concentrated on the bottom part of the image. We can also observe relatively high errors on the regions where vegetation abundances are small.
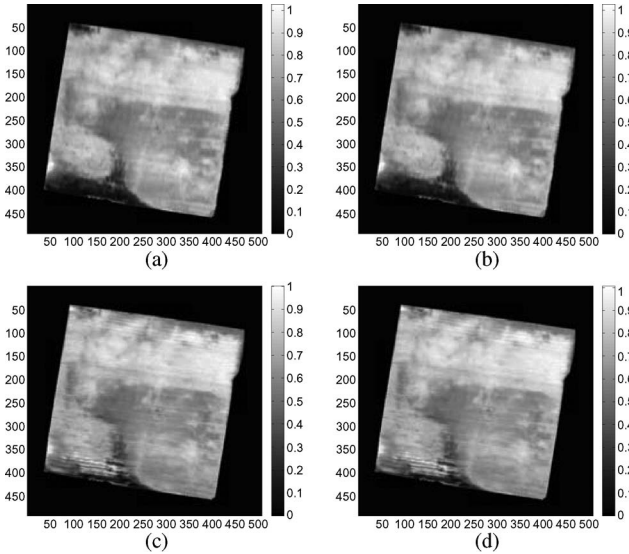
Fig. 8. Abundances of the vegetation endmembers extracted by using VCA and N-Finder on the image of Field 2 taken on 18 May 2001 (top row) and 29 May 2001 (bottom row). The abundances are estimated with non-negative condition [see (2)].

Fig. 9. Abundances of the vegetation endmembers extracted by using VCA and N-Finder on the image of **Field 2** taken on 18 May 2001 (top row) and 29 May 2001 (bottom row). The abundances are estimated with non-negative and sum-to-one conditions [see (3)].

B. Results on Field 2

In Fig. 7(a) and (b), we show the spectra of the two endmembers extracted by using VCA and N-Finder on the image of Field 2 taken on the date 18 May 2001. It can be seen that the second endmember extracted by VCA and the first endmember extracted by N-Finder correspond to vegetation. In Fig. 7(c) and (d), we show the spectra of the two endmembers extracted by using VCA and N-Finder on the image of Field 2 taken on the date 29 May 2001. It can be seen that the first endmembers extracted by both methods correspond to vegetation.

With the help of the spectra of the extracted endmembers, we then compute the abundances of these endmembers by using (2). In Fig. 8, we show the abundance maps of the endmembers extracted by VCA and N-Finder on the image of Field 2 taken on the dates of 18 May 2001 and 29 May 2001.

In Fig. 9, we show the abundance maps of the vegetation endmembers computed by (3) on the image of Field 2 taken on the dates 18 May 2001 and 29 May 2001.

We then compute the correlation coefficients between the crop yield map of Field 2 with the (combined) vegetation abundances computed by (4)–(17). The results are shown in Table II.

For Field 2, we can draw nearly the same remarks as for the Field 1:

- The abundance maps of vegetation computed with only non-negative condition are more strongly correlated to the yield map than the abundances computed with both non-negative and sum-to-one conditions.
- The performances of VCA and N-Finder are very similar. The results given by VCA are slightly better than N-Finder.
- By combining the vegetation abundances of the two dates, the correlation coefficients improve. Even though for this field, the correlation coefficients between the yield map
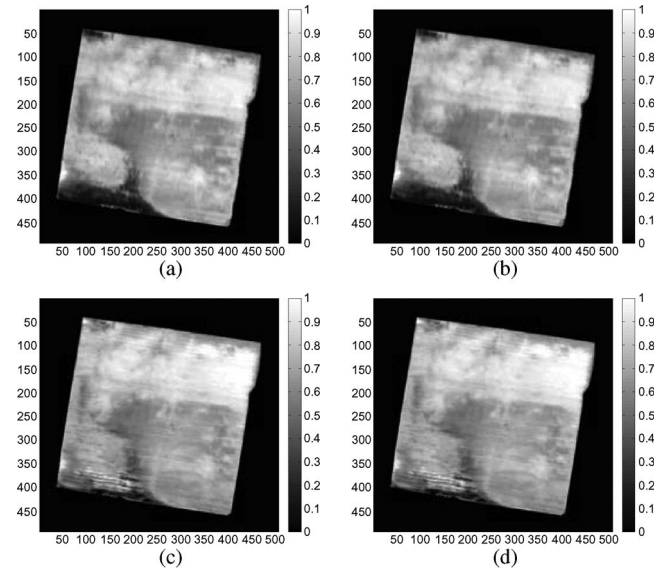
and the abundance maps obtained on one single date are relatively low, however, by combining the vegetation abundances of the two dates, the highest correlation coefficients are around 0.74, which is very close to the best results obtained by the supervised unmixing approach presented in [23].

- The highest correlation coefficients are again obtained by M_4 and M_{10} when the endmembers are extracted by VCA and the abundances are estimated with only non-negative condition (see (2)), which is the same as for Field 1.

In Fig. 10(a) and (b), we show the combined vegetation abundances computed on Field 1 of which the correlation coefficients are the highest (M_4 and M_{10} when the endmembers are extracted by VCA and the abundances are computed with only non-negative condition).

We then fit the two combined vegetation abundances (M_4 and M_{10}) with the yield map by linear regression. More concretely, we compute the fitted model $\hat{Y}_i(k)$ by (19). The absolute error between $\hat{Y}_4(k)$ (resp. $\hat{Y}_{10}$) and the yield map $Y(k)$ by $E_4(k) = |\hat{Y}_4(k) - Y(k)|$ (resp. $E_{10}(k) = |\hat{Y}_{10}(k) - Y(k)|$), which is shown in Fig. 10(c) [resp. 10(d)].

It can be seen that nearly all the errors are concentrated on the regions where vegetation abundances are small, which is coherent with the reults obtained for Field 1. This may be due to the fact that, on the regions where the vegetation abundances are small, there are more nonlinear effects (multiple scattering for example) between the vegetation and the bare soil. Linear unmixing approaches cannot precisely estimate the vegetation abundances on these regions.

VII. COMPARISON WITH ADVANCED TECHNIQUES FOR LINEAR ENDMEMBER EXTRACTION

In this section, two advanced techniques for linear endmember extraction are evaluated. At first, we evaluate the

TABLE II
CORRELATION COEFFICIENTS BETWEEN THE INTERPOLATED CROP YIELD MAP AND THE (COMBINED) VEGETATION ABUNDANCES COMPUTED BY (4)–(17) ON THE IMAGE OF **Field 2**. FOR FIRST THREE COLUMNS, THE ABUNDANCES ARE COMPUTED WITH NON-NEGATIVE CONDITION. WHILE FOR LAST THREE COLUMNS, THE ABUNDANCES ARE COMPUTED WITH BOTH NON-NEGATIVE AND SUM-TO-ONE CONDITIONS

|	M_1	M_2	M_3	M_4	M_5	M_6	M_7	M_8	M_9	M_{10}	M_{11}	M_{12}	M_{13}
Non-negative condition													
VCA	0.648	0.721	0.712	0.743	0.739	0.735	0.701	0.723	0.715	0.748	0.742	0.720	0.735
N-Finder	0.646	0.706	0.703	0.734	0.730	0.725	0.691	0.700	0.690	0.729	0.723	0.657	0.691
Non-negative and sum-to-one conditions													
VCA	0.649	0.650	0.681	0.705	0.701	0.697	0.670	0.693	0.686	0.715	0.710	0.666	0.687
N-Finder	0.649	0.648	0.680	0.704	0.701	0.697	0.669	0.694	0.686	0.717	0.712	0.669	0.690
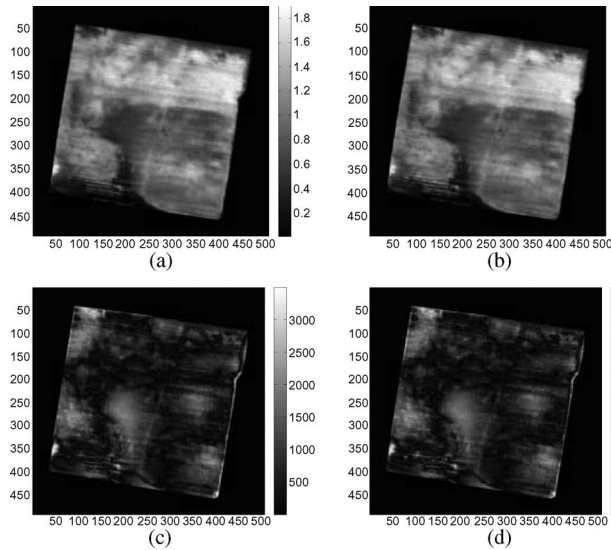
Fig. 10. (a) M_4 and (b) M_{10} computed on **Field 2**. The endmembers are extracted by VCA, and the abundances are computed with (2). They are the most correlated with the yield map of Field 2. (c) and (d) Absolute error between the yield map and the fitted model $\hat{Y}_4, \hat{Y}_{10}$ [see (19)].
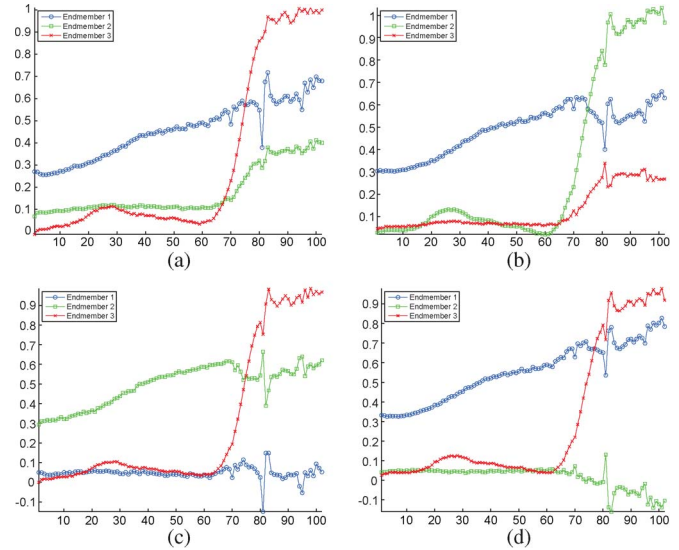

Fig. 11. Spectra of the two endmembers extracted by using MVSA on (a) and (b) **Field 1** and (c) and (d) **Field 2** taken on the dates 18 May 2001 and 29 May 2001.

advanced extraction method MVSA [35] which does not require pure pixel for each endmember. Afterwards, the spatial preprecessing presented in [36] which can enhance the endmember for improving the extraction results is evaluated.

A. Minimum Volume Simplex Analysis (MVSA)

In contrary to the direct methods (such as VCA, n-Finder, SMACC, etc.), the advanced endmember extraction methods (e.g., MVSA, SISAL, etc.) extract the extrema of the optimal simplex containing the hyperspectral data as the endmembers, which do not require pure pixels. In order to investigate whether the pure pixel assumption plays an important role in our study, the MVSA [35] is evaluated in this section. MVSA tries to find the simplex with minimal volume which enclose all the hyperspectral data points and extracts the extrema of the minimal simplex as endmembers. During the experiments, it has been found that, for the MVSA method, it is necessary to extract three endmembers rather than two endmembers to obtain satisfactory estimation results.

In Fig. 11, the spectra of the endmembers extracted by MVSA on Field 1 and Field 2 are shown. For Field 1, the third (resp. the second) endmember extracted on the date 18 May 2001 (resp. 29 May 2001) corresponds to the well to the vegetation. While for the Field 2, the third endmembers extracted on the both date correspond well to the vegetation.

As usual, the abundances of the extracted endmembers are again estimated by using both NNLS [(2)] and FCLS [(3)]. The vegetation abundances estimated on the two different dates are combined by using the (4)–(17). The correlation coefficients between the (combined) vegetation abundances and the crop yield maps of the two fields are then computed of which the results are shown in Table III.

The correlation coefficients between the yield map and the (combined) vegetation abundances of Field 1 are very low because among the three endmembers extracted by the MVSA method on Field 1, there are two which are similar to vegetation (the second and the third endmembers extracted from the images of the both dates). This may be caused by the fact that there is very few bare soil on Field 1. As we have mentionned at the beginning of this section, if we extract too few endmembers, the optimal simplex obtained by MVSA may not contain the pixels of bare soil. And the endmember corresponding to bare soil may be considered as noise by MVSA. Therefore, in order to obtain bare soil, it is necessary to extract more endmembers (in this case we extract three). Inevitably, one endmember corresponds to bare soil, one corresponds to vegetation, and the third one is intermediate.

TABLE III
CORRELATION COEFFICIENTS BETWEEN THE INTERPOLATED CROP YIELD MAP AND THE (COMBINED) VEGETATION ABUNDANCES COMPUTED BY (4)–(17) ON **Field 1** AND **Field 2**. THE ENDMEMBERS ARE EXTRACTED BY **MVSA**. THE ABUNDANCE MAPS ARE, RESPECTIVELY, COMPUTED BY USING NON-NEGATIVE CONDITION (NNLS) AND BY USING BOTH NON-NEGATIVE CONDITION AND SUM-TO-ONE CONDITION (FCLS)

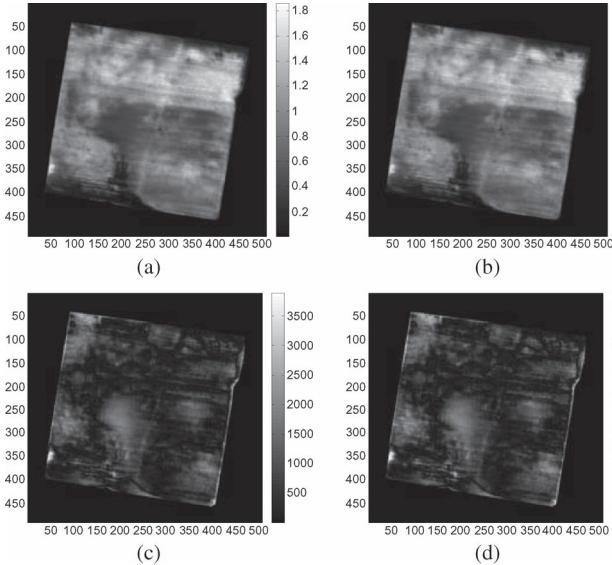| Field 1													
	M_1	M_2	M_3	M_4	M_5	M_6	M_7	M_8	M_9	M_{10}	M_{11}	M_{12}	M_{13}
NNLS	0.634	0.551	0.623	0.642	0.637	0.633	0.615	0.624	0.616	0.642	0.634	0.568	0.572
FCLS	0.714	0.574	0.667	0.680	0.675	0.670	0.661	0.666	0.661	0.679	0.670	0.602	0.610
Field 2													
	M_1	M_2	M_3	M_4	M_5	M_6	M_7	M_8	M_9	M_{10}	M_{11}	M_{12}	M_{13}
NNLS	0.650	0.715	0.718	0.753	0.751	0.748	0.709	0.727	0.720	0.758	0.755	0.713	0.738
FCLS	0.650	0.761	0.737	0.775	0.772	0.768	0.727	0.745	0.737	0.781	0.775	0.740	0.771

Fig. 12. (a) M_4 and (b) M_{10} computed on Field 2. They are the most correlated with the yield map of Field 2. The endmembers are extracted by MVSA. The abundances maps are computed by FCLS. (c) and (d) Absolute error between the yield map and the fitted model $\hat{Y}_4, \hat{Y}_{10}$ [see (19)].
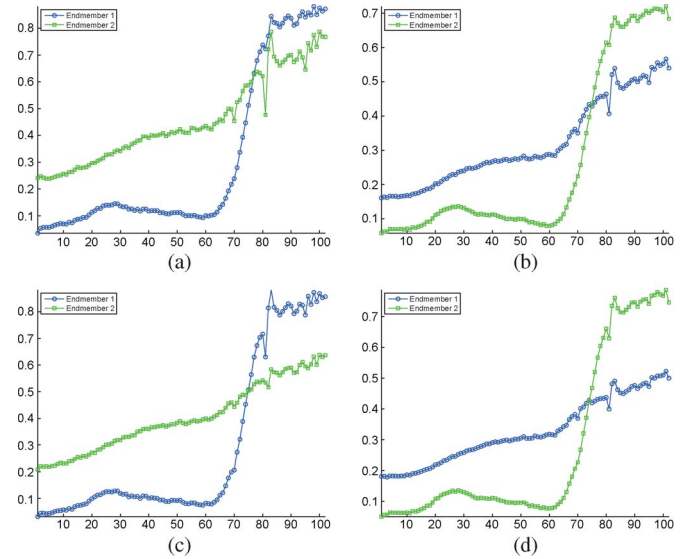

Fig. 13. Spectra of the two endmembers extracted by using VCA after spatial preprocessing on (a) and (b) **Field 1** and (c) and (d) **Field 2** taken on the dates 18 May 2001 and 29 May 2001.

In contrary to Field 1, the MVSA method has extracted only one vegetation endmember on each of the image because there is more bare soil than Field 2. The (combined) vegetation abundances are highly correlated to the yield map when compared to the results of Field 1. It can also be seen that M_4 and M_{10} still the most correlate to the yield map. In Fig. 12, we show the M_4 and M_{10} as well as the absolute error between the yield map and the fitted model $\hat{Y}_4, \hat{Y}_{10}$ [see (19)] for Field 2. The abundances are computed by both non-negative and sum-to-one condition (FCLS). It can be seen that again the absolute errors are concentrated on the regions where the vegetation abundances are low. This is coherent to the results obtained in the previous section by using direct endmember extraction approaches, such as VCA (see Fig. 10), because the errors appear at the regions where the nonlinear mixtures are important and the methods based on linear mixture assumption are not adaptive.

B. Spatial Preprocessing

It has to be remarked that, the direct methods and the advanced methods for endmember extraction are both pixel-wise. They do not take spatial information into consideration, which could be important, since structures are present in images. The authors of [36] have proposed a preprocessing of hyperspectral images in order to cooperate spatial information into the endmember extraction, and this preprocessing can effectively improve the extraction results. The authors compute for each pixel a weight scalar value according to the similarity of the pixel with its neighborhood inside an analyze window with $ws \times ws$ size. We apply this spatial preprocessing on the hyperspectral images of Field 1 and Field 2. On these preprocessed images, the endmembers are then extracted by using VCA. The size of the analyze window is 3×3.

In Fig. 13, the spectra of the endmembers extracted by VCA after spatial preprocessing are shown. As usual, the abundances of the extracted endmembers are again estimated by using both NNLS [(2)] and FCLS [(3)]. The vegetation abundances estimated on the two different dates are combined by using the (4)–(17). The correlation coefficients between the (combined) vegetation abundances and the crop yield maps of the two fields are then computed of which the results are shown in Table IV.

Because spatial preprocessing can very well enhance the spectra of real endmembers in homogeneous regions (which is quite useful for our data sets, since the spatial resolution is quite high and the fields are homogeneous), there is an overall improvement for nearly all the correlation coefficients between the (combined) vegetation abundances and the yield maps. In particular, for Field 2, the correlation coefficients obtained by the abundances computed with FCLS are even

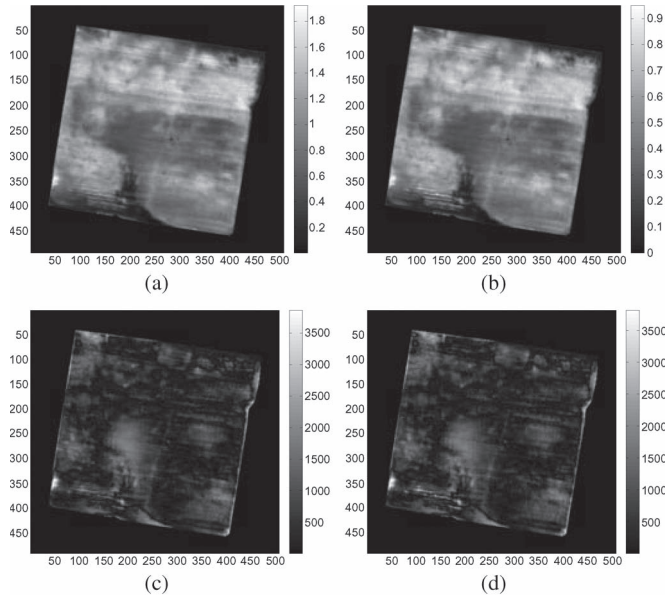| Field 1												
	M_1	M_2	M_3	M_4	M_5	M_6	M_7	M_8	M_9	M_{10}	M_{11}	M_{12}	M_{13}
NNLS	0.723	0.755	0.765	0.775	0.774	0.774	0.764	0.768	0.767	0.777	0.777	0.725	0.738
FCLS	0.526	0.757	0.708	0.717	0.731	0.743	0.721	0.745	0.756	0.754	0.776	0.763	0.760
Field 2												
	M_1	M_2	M_3	M_4	M_5	M_6	M_7	M_8	M_9	M_{10}	M_{11}	M_{12}	M_{13}
NNLS	0.705	0.758	0.757	0.776	0.775	0.774	0.755	0.762	0.760	0.778	0.777	0.747	0.760
FCLS	0.751	0.763	0.785	0.810	0.810	0.809	0.784	0.782	0.780	0.807	0.808	0.752	0.767

Fig. 14. (a) M_4 and (b) M_{10} computed on Field 2. They are the most correlated with the yield map of Field 2. The endmembers are extracted by VCA after spatial preprocessing. The abundances maps are computed by FCLS. (c) and (d) Absolute error between the yield map and the fitted model $\hat{Y}_4, \hat{Y}_{10}$ [see (19)].

greater than 0.8. Another observation is that again the best correlation coefficients are obtained by the M_4 and M_{10}, which is coherent to all the previous results. In Fig. 14, we show the M_4 and M_{10} as well as the absolute error between the yield map and the fitted model $\hat{Y}_4, \hat{Y}_{10}$ [see (19)] for Field 2. The abundances are computed by both non-negative and sum-to-one condition (FCLS). It can be seen that still the absolute errors are concentrated on the regions where the vegetation abundances are low. Because as explained in the previous section, though the spatial preprocessing has been applied, the endmembers are still extracted with linear mixture models. And nonlinearities present on these regions.

VIII. CONCLUSION

In this paper, we have evaluated two direct unsupervised linear unmixing approaches (VCA and N-Finder) for the application of crop yield estimation. The results show that abundance maps of the vegetation extracted by both approaches are strongly correlated to the yield data (the correlation coefficients are between 0.7 to 0.8). When compared to the traditional supervised approach presented in [23], which needs reference

spectra obtained either by measurements in laboratory or manual selection from the image, in this paper, the spectra of the endmembers are automatically extracted. The results validate the higher efficiency of the unsupervised unmixing approaches. The spectra measured in laboratory cannot perfectly represent the spectra of the endmembers on the field, because the observation conditions cannot be exactly simulated. The hyperspectral images have a huge amount of pixels, it is very difficult to manually select the best spectra of vegetation and bare soil. Therefore, unsupervised endmember extraction methods can obtain better results than the supervised approach.

In addition, the unmixing was performed on the hyperspectral images of the same fields, but taken on different dates. The results show that the correlations between the vegetation abundances, and the yield map might change in terms of the observation dates. However, by combining the vegetation abundances extracted on different dates, the correlations are improved so that we can always obtain the highest correlations. And the weigthed sums of the squares of the vegetation abundances estimated on the two dates are the most correlated to the yield data.

Finally, two advanced endmember extraction techniques, methods without pure pixel assumption (MVSA) and spatial preprocessing, have also been evaluated. The results show that the MVSA method cannot significantly improve the correlation between the vegetation abundances and the crop yield map. While the spatial preprocessing, which can enhance the spectra of the endmembers inside homogeneous regions, has achieved an overall improvement. However, since all the used unmixing methods are based on linear mixture models, estimation errors are always concentrated on the regions where strong nonlinear effects present. These effects would be interesting for the further investigation.

REFERENCES

[1] P. S. Thenkabail, A. D. Ward, and J. G. Lyon, "Landsat-5 thermatic mapper models of soybean and corn crop characteristics," *Int. J. Remote Sens.*, vol. 15, no. 1, pp. 49–61, 1995.

[2] A. Gitelson, A. Vina, J. Masek, S. Verma, and A. Suyker, "Synoptic monitoring of gross primary productivity of maize using Landsat data," *IEEE Geosci. Remote Sens. Lett.*, vol. 5, no. 2, pp. 133–137, Apr. 2008.

[3] J. A. J. Berni, P. J. Zarco-Tejada, L. Suarez, and E. Fereres, "Thermal and narrowband multispectral remote sensing for vegetation monitoring from an unmanned aerial vehicle," *IEEE Trans. Geosci. Remote Sens.*, vol. 47, no. 3, pp. 722–738, Mar. 2009.

[4] A. A. Ursani, K. Kpalma, C. C. D. Lelong, and J. Ronsin, "Fusion of textural and spectral information for tree crop and other agricultural cover mapping with very-high resolution satellite images," *IEEE J. Sel. Topics Appl. Earth Observ. Remote Sens.*, vol. 5, no. 1, pp. 225–235, Feb. 2012.

[5] J. Rouse, R. Haas, J. Shell, and D. Deering, "Monitoring vegetation systems in the great plains with ERTS-1," in *Proc. 3rd Earth Resources Technol. Satell. Symp.*, Washington, DC, 1973, vol. 1, pp. 309–317, Goddard Space Flight Center.

[6] S. Groten, "Ndvi-crop monitoring and early yield assessment of Burkina Faso," *Int. J. Remote Sens.*, vol. 14, no. 8, pp. 1495–1515, 1993.

[7] C. L. Wiegand, A. J. Richardson, D. E. Escobar, and A. H. Gerbermann, "Vegetation indices in crop assessments," *Remote Sens. Environ.*, vol. 35, no. 2/3, pp. 105–119, 1991.

[8] R. E. Plant, D. Munk, B. Roberts, R. Vargas, D. Rains, R. Travis, and R. Hutmacher, "Relationships between remotely sensed reflectance data and cotton growth and yield," *Trans. ASAE*, vol. 43, no. 3, pp. 535–564, 2000.

[9] C. Yang, J. H. Everitt, and J. M. Bradford, "Relationships between yield monitor data and airborne multidate multispectral digital imagery for grain sorghum," *Precision Agricult.*, vol. 3, no. 4, pp. 373–388, 2002.

[10] P. Basnyat, B. McConkey, B. Meinert, C. Gatkze, and G. Noble, "Agriculture field characterization using aerial photograph and satellite imagery," *IEEE Geosci. Remote Sens. Lett.*, vol. 1, no. 1, pp. 7–10, Jan. 2004.

[11] Y. Uno, S. Prasher, R. Lacroix, P. Goel, Y. Karimi, A. Viau, and R. Patel, "Artificial neural networks to predict corn yield from compact airborne spectrographic imager data," *Comput. Electron. Agricult.*, vol. 47, no. 2, pp. 149–161, May 2005.

[12] O. Wendroth, H. Reuter, and K. Kersebaum, "Predicting yield of barley across a landscape: A state-space modeling approach," *J. Hydrol.*, vol. 272, no. 1–4, pp. 250–263, Mar. 2003.

[13] A. Bannari, K. S. Khurshid, K. Staenz, and J. W. Schwarz, "A comparison of hyperspectral chlorophyll indices for wheat crop chlorophyll content estimation using laboratory reflectance measurements," *IEEE Trans. Geosci. Remote Sens.*, vol. 45, no. 10, pp. 3063–3074, Oct. 2007.

[14] D. Haboudane, N. Tremblay, J. Miller, and P. Vigneault, "Remote estimation of crop chlorophyll content using spectral indices derived from hyperspectral data," *IEEE Trans. Geosci. Remote Sens.*, vol. 46, no. 2, pp. 423–437, Feb. 2008.

[15] K. Richter, C. Atzberger, F. Vuolo, and G. D'Urso, "Evaluation of sentinel-2 spectral sampling for radiative transfer model based lai estimation of wheat, sugar beet, and maize," *IEEE J. Sel. Topics Appl. Earth Observ. Remote Sens.*, vol. 4, no. 2, pp. 458–464, Jun. 2011.

[16] W. A. Dorigo, "Improving the robustness of cotton status characterisation by radiative transfer model inversion of multi-angular CHRIS/PROBA data," *IEEE J. Sel. Topics Appl. Earth Observ. Remote Sens.*, vol. 5, no. 1, pp. 18–29, Feb. 2012.

[17] P. S. Thenkabail, R. B. Smith, and E. D. Pauw, "Hyperspectral vegetation indices and their relations with agricultural crop characteristics," *Remote Sens. Environ.*, vol. 71, no. 2, pp. 158–182, Feb. 2000.

[18] P. Goel, S. Prasher, J. Landry, R. M. Patel, A. Viau, and J. Miller, "Estimation of crop biophysical parameters through airborne and field hyperspectral remote sensing," *Trans. ASAE*, vol. 46, no. 4, pp. 1235–1246, 2003.

[19] P. Zarco-Tejada, S. Ustin, and M. Whiting, "Temporal and spatial relationships between within-field yield variability in cotton and high-spatial hyperspectral remote sensing imagery," *Agronomy J.*, vol. 97, no. 3, pp. 641–653, 2005.

[20] A. Li, S. Liang, A. Wang, and J. Qin, "Estimating crop yield from multitemporal satellite data using multivariate regression and neural network techniques," *Photogramm. Eng. Remote Sens.*, vol. 73, no. 10, pp. 1149–1157, Oct. 2007.

[21] B. Luo, C. Yang, and J. Chanussot, "Unsupervised linear unmixing of hyperspectral image for crop yield estimation," in *Proc. IEEE IGARSS*, Honolulu, HI, 2010, pp. 185–188.

[22] A. Plaza, J. A. Benediktsson, J. Boardman, J. Brazile, L. Bruzzone, G. Camps-Valls, J. Chanussot, M. Fauvel, P. Gamba, A. Gualtieri, M. Marconcini, J. C. Tilton, and G. Trianni, "Recent advances in techniques for hyperspectral image processing," *Remote Sens. Environ.*, vol. 113, no. 1, pp. S110–S122, Sep. 2009.

[23] C. Yang, J. H. Everitt, and J. M. Bradford, "Airborne hyperspectral imagery and linear spectral unmixing for mapping variation in crop yield," *Precision Agricult.*, vol. 8, no. 6, pp. 279–296, Dec. 2007.

[24] M. Parente and A. Plaza, "Survey of geometric and statistical unmixing algorithms for hyperspectral images," in *Proc. IEEE WHISPERS*, Reykjavik, Iceland, 2010, pp. 1–4.

[25] J. Nascimento and J. B. Dias, "Does independent component analysis play a role in unmixing hyperspectral data," *IEEE Trans. Geosci. Remote Sens.*, vol. 43, no. 1, pp. 175–187, Jan. 2005.

[26] S. Moussaoui, H. Hauksdóttir, F. Schmidt, C. Jutten, J. Chanussot, D. Brie, S. Douté, and J. Benediktsson, "On the decomposition of mars hyperspectral data by ICA and bayesian positive source separation," *Neurocomputing*, vol. 71, no. 10–12, pp. 2194–2208, Jun. 2008.

[27] J. M. Bioucas-Dias, A. Plaza, N. Dobigeon, M. Parente, Q. Du, P. Gader, and J. Chanussot, "Hyperspectral unmixing overview: Geometrical, statistical, and sparse regression-based approaches," *IEEE J. Sel. Topics Appl. Earth Observ. Remote Sens.*, vol. 5, no. 2, pp. 354–379, Apr. 2012.

[28] I. Dópido, A. Villa, A. Plaza, and P. Gamba, "A quantitative and comparative assessment of unmixing-based feature extraction techniques for hyperspectral image classification," *IEEE J. Sel. Topics Appl. Earth Observ. Remote Sens.*, vol. 5, no. 2, pp. 421–435, Apr. 2012.

[29] M. E. Winter, "Fast autonomous spectral end-member determination," in *Proc. 13th Int. Conf. Appl. Geol.*, Vancouver, BC, Canada, 1999, vol. 2, pp. 337–344.

[30] J. Nascimento and J. B. Dias, "Vertex component analysis: A fast algorithm to unmix hyperspectral data," *IEEE Trans. Geosci. Remote Sens.*, vol. 43, no. 4, pp. 898–910, Apr. 2005.

[31] J. Gruninger, A. J. Ratkowski, M. L. H. S. S. Shen, and P. E. Lewis, "The sequential maximum angle convex cone (smacc) endmember model," in *Proc. SPIE—Algorithms Technologies Multispectral, Hyperspectral, Ultraspectral Imagery X*, 2004, vol. 5425, pp. 1–14.

[32] L. Miao and H. Qi, "Endmember extraction from highly mixed data using minimum volume constrained nonnegative matrix factorization," *IEEE Trans. Geosci. Remote Sens.*, vol. 45, no. 3, pp. 765–777, Mar. 2007.

[33] T. Chan, C. Chi, Y. Huang, and W. Ma, "A convex analysis-based minimum-volume enclosing simplex algorithm for hyperspectral unmxing," *IEEE Trans. Signal Process.*, vol. 57, no. 11, pp. 4418–4432, Nov. 2009.

[34] J. Bioucas-Dias, "A variable splitting augmented lagrangian approach to linear spectral unmixing," in *Proc. 1st IEEE WHISPERS*, Grenoble, France, 2009, pp. 1–4.

[35] J. Li and J. M. Bioucas-Dias, "Minimum volume simplex analysis: A fast algorithm to unmix hyperspectral data," in *Proc. IGARSS*, Boston, MA, 2008, vol. 3, pp. III-250–III-253.

[36] M. Zortea and A. Plaza, "Spatial preprocessing for endmember extraction," *IEEE Trans. Geosci. Remote Sens.*, vol. 47, no. 8, pp. 2679–2693, Aug. 2009.

[37] J. W. Boardman, F. A. Fruse, and R. O. Green, "Mapping target signatures via partial unmixing of aviris data," in *Proc. 5th JPL Airborne Earth Sci. Workshop*, 1995, vol. 95, pp. 23–26.

[38] C. Yang, J. H. Everitt, M. R. David, and C. Mao, "A CCD camera-based hyperspectral imaging system for stationary and airborne applications," *Geocarto Int.*, vol. 18, no. 2, pp. 71–80, Jun. 2003.

Bin Luo received the M.Sc. degree from ENS Cachan, France, in 2003, and the Ph.D. degree from ENST Paris, France, in 2007.

He worked as a Post Doctoral Researcher in Grenoble Images Speech Signals and Automatics Laboratory, Grenoble, France, from 2008 to 2010. Currently, he is an Associate Professor in the State Key Laboratory of Information Engineering in Surveying, Mapping, and Remote Sensing (LIESMARS) at Wuhan University, Wuhan, China. His research interests include hyperspectral data analysis and high-resolution remote sensing image processing.

Chenghai Yang received the B.S. and M.S. degrees in agricultural engineering from Northwest A&F University, Xianyang, China, and the Ph.D. degree in agricultural engineering from the University of Idaho, Moscow.

He is an Agricultural Engineer with the USDA Agricultural Research Service's Southern Plains Agricultural Research Center, College Station, TX. His current research is focused on the use of remote sensing and other spatial information technologies for precision agriculture and pest management. He is a Member of four professional societies and serves as an Editor or Associate Editor for five technical journals. He has authored or coauthored numerous journal articles and other technical publications. He is recognized nationally and internationally for his research on airborne multispectral and hyperspectral remote sensing for agricultural applications.

Jocelyn Chanussot (M'04–SM'04–F'12) received the M.Sc. degree in electrical engineering from the Grenoble Institute of Technology (Grenoble INP), Grenoble, France, in 1995, and the Ph.D. degree from Savoie University, Annecy, France, in 1998.

In 1999, he was with the Geography Imagery Perception Laboratory for the Delegation Generale de l'Armement (French National Defense Department). Since 1999, he has been with Grenoble INP, where he was an Assistant Professor from 1999 to 2005, an Associate Professor from 2005 to 2007, and is currently a Professor of signal and image processing. He is currently conducting his research at the Grenoble Images Speech Signals and Automatics Laboratory. His research interests include image analysis, multicomponent image processing, nonlinear filtering, and data fusion in remote sensing.

Dr. Chanussot is the Founding President of IEEE Geoscience and Remote Sensing French chapter (2007–2010) which received the 2010 IEEE GRS-S Chapter Excellence Award "for excellence as a Geoscience and Remote Sensing Society chapter demonstrated by exemplary activities during 2009." He was the recipient of the NORSIG 2006 Best Student Paper Award, the IEEE GRSS 2011 Symposium Best Paper Award and of the IEEE GRSS 2012 Transactions Prize Paper Award. He was a Member of the IEEE Geoscience and Remote Sensing Society AdCom (2009–2010), in charge of membership development. He was the General Chair of the first IEEE GRSS Workshop on Hyperspectral Image and Signal Processing, Evolution in Remote sensing. He is the Chair (2009–2011) and was the Cochair of the GRS Data Fusion Technical Committee (2005–2008). He was a Member of the Machine Learning for Signal Processing Technical Committee of the IEEE Signal Processing Society (2006–2008) and the Program Chair of the IEEE International Workshop on Machine Learning for Signal Processing, (2009). He was an Associate Editor for the IEEE GEOSCIENCE AND REMOTE SENSING LETTERS (2005–2007) and for *Pattern Recognition* (2006–2008). Since 2007, he has been an Associate Editor for the IEEE TRANSACTIONS ON GEOSCIENCE AND REMOTE SENSING. Since 2011, he has been the Editor-in-Chief of the IEEE JOURNAL OF SELECTED TOPICS IN APPLIED EARTH OBSERVATIONS AND REMOTE SENSING.

Liangpei Zhang (M'06–SM'08) received the B.S. degree in physics from Hunan Normal University, Changsha, China, in 1982, the M.S. degree in optics from the Xi'an Institute of Optics and Precision Mechanics, Chinese Academy of Sciences, Xi'an, China, in 1988, and the Ph.D. degree in photogrammetry and remote sensing from Wuhan University, Wuhan, China, in 1998.

He is currently the Head of the Remote Sensing Division, State Key Laboratory of Information Engineering in Surveying, Mapping, and Remote Sensing, Wuhan University. He is also a "Chang-Jiang Scholar" Chair Professor appointed by the Ministry of Education of China. Currently, he is a Principal Scientist for the China State Key Basic Research Project (2011–2016) appointed by the Ministry of National Science and Technology of China to lead the remote sensing program in China. He has more than 240 research papers. He is the holder of five patents. His research interests include hyperspectral remote sensing, high-resolution remote sensing, image processing, and artificial intelligence.

Dr. Zhang is a Fellow of the IEE, Executive Member (Board of Governor) of the China National Committee of International Geosphere-Biosphere Programme, Executive Member of the China Society of Image and Graphics, etc. He regularly serves as a Cochair of the series SPIE Conferences on Multispectral Image Processing and Pattern Recognition, Conference on Asia Remote Sensing, and many other conferences. He edits several conference proceedings, issues, and geoinformatics symposiums. He also serves as an Associate Editor of the *International Journal of Ambient Computing and Intelligence, International Journal of Image and Graphics, International Journal of Digital Multimedia Broadcasting, Journal of Geospatial Information Science*, and *Journal of Remote Sensing*.